

Exponential Quantum Speedup on Structured Hard Instances of Maximum Independent Set

V. Choi
Gladiolus Veritatis Consulting Co.*

January 27, 2026

Establishing quantum speedup for computationally hard problems of practical relevance, particularly combinatorial optimization problems, remains a central challenge in quantum computation. In this work, we identify a structurally defined family of classically hard maximum independent set (MIS) instances, and design and analyze a non-stoquastic adiabatic quantum optimization algorithm that exploits this structure. The algorithm runs in polynomial time and achieves an exponential speedup over both transverse-field quantum annealing and state-of-the-art classical solvers on these instances, under assumptions supported by analytical and numerical evidence. We identify the essential quantum mechanism enabling the speedup as the use of a non-stoquastic XX -driver to access a larger sign-structured admissible subspace beyond the stoquastic regime, which allows sign-generating quantum interference to create smooth evolution paths that bypass tunneling. This identifies a distinctive quantum mechanism underlying the speedup and explains why no efficient classical analogue is likely to exist. In addition, our analysis produces scalable small-scale models, derived from our structural reduction, that capture the essential dynamics of the algorithm. These models provide a concrete opportunity for verification of the quantum advantage mechanism on currently available universal quantum computers.

1 Introduction

Breakthrough work by Shor (1) demonstrated the potential of quantum computation to achieve exponential speedup for problems believed to be classically intractable. One of the broad attractions of quantum computation is its potential to address NP-hard combinatorial optimization problems, which are widely believed to be intractable for classical computers. However, since Shor’s result, provable and practically relevant quantum speedups have predominantly been realized in quantum simulation; see, e.g., the references in (2). Despite substantial effort, much of the work on quantum optimization has emphasized heuristic or hybrid approaches rather than rigorous speedup guarantees. As a result, provably advantageous quantum algorithms for practically relevant optimization problems have remained elusive; see, e.g., (3, 4).

In this work, we identify a structurally defined family of classically hard maximum independent set (MIS) instances, referred to as GIC graphs. We design and analyze a non-stoquastic adiabatic quantum optimization algorithm, called Dic-Dac-Doa¹, first proposed in 2021 (5). The algorithm runs in polynomial time and achieves exponential speedup over both transverse-field quantum annealing (TFQA) and classical algorithms on GIC graphs, under assumptions supported by analytical and numerical evidence. The underlying structural principles of the graphs are not contrived, but capture intrinsic sources of hardness in MIS, and can be extended to broader classes of instances, including those relevant to real-world applications. This contribution directly corresponds to two central stages emphasized by Babbush *et al.*: “the identification of concrete problem instances expected to exhibit quantum advantage (Stage II) and the connection of such instances to real-world use cases (Stage III)” (2).

*<https://www.vc-gladius.com>

¹The acronym originally stood for *Driver graph from Independent Cliques, Double Anti-Crossing, Diabatic quantum Optimization Annealing*.

The MIS problem is a canonical NP-hard combinatorial optimization problem (6) and has served as a central benchmark for quantum optimization. Indeed, quantum hardware has been designed specifically for solving MIS problems (7–10).

Adiabatic quantum computing (AQC) was originally proposed as a general-purpose framework for solving optimization problems (11–13). It was later shown to be polynomially equivalent to the standard circuit model of quantum computation (14). Implementing an adiabatic quantum algorithm on a gate-based quantum computer is referred to as digitized AQC (15). In AQC, the system is initialized in the ground state of a simple Hamiltonian and slowly evolved toward a final Hamiltonian encoding the problem of interest. While this analog paradigm is conceptually simple from an algorithmic design perspective, rigorous analysis of its computational performance, in particular its runtime scaling, has proven challenging. In practice, adiabatic quantum algorithm (or quantum annealing) has most often been treated as a heuristic, black-box optimization paradigm, in which little problem-specific structure is incorporated into the algorithmic design, and performance is typically assessed empirically rather than through analytical characterization.

Here, we show how to explicitly incorporate problem structure into the design and analysis of a quantum optimization algorithm, and develop an analytical framework for characterizing its performance. Our approach departs from the traditional spectral-gap perspective (16) and instead measures the efficiency of the algorithm by the presence or absence of an anti-crossing (see Section 5 of Supplement for a precise definition). The key idea is to infer this behavior directly from the crossing properties of bare energy levels of relevant subsystems, without explicitly constructing the effective two-level Hamiltonian.

The Dic-DAC-DoA algorithm modifies standard TFQA by adding a specially designed non-stoquastic XX-driver term, aimed at overcoming the small-gap anti-crossings that plague TFQA on GIC graphs. Despite their structured construction, we argue that GIC graphs exhibit classical hardness: solving MIS on such instances would require exponential time unless $P = NP$. We provide numerical results using state-of-the-art classical solvers on representative instances. We further conjecture that no tailored classical algorithm can solve these structured instances efficiently.

This raises a natural question: what quantum resource enables Dic-DAC-DoA to succeed on instances that remain intractable for both TFQA and classical algorithms? As also emphasized in (15), non-stoquastic Hamiltonians may play an essential role in AQC, both for universality and for improved performance on hard optimization problems.

Here, we explicitly identify the essence of going beyond stoquasticity: the ability to exploit a larger sign-structured subspace, which enables new evolution paths that are dynamically inaccessible in the stoquastic regime. This mechanism is fundamentally different from the conventional view that quantum speedup in Hamiltonian-based optimization arises from quantum tunneling. This perspective is rooted in a fundamental feature of quantum mechanics: the wavefunction of a quantum state, expressed in a given basis, can have both positive and negative amplitudes, in contrast to classical probabilities, which must be non-negative. We therefore introduce terminology to characterize sign structure. A quantum state expressed in a given basis is said to be *same-sign* if all amplitudes in that basis are non-negative, and *opposite-sign* if it contains both positive and negative amplitudes; see Section 1 of Supplement for a precise definition. Correspondingly, a basis is called same-sign if it consists entirely of same-sign states, and opposite-sign otherwise. Subspaces/sectors and matrix blocks are classified according to the sign structure of the basis in which they are expressed.

For stoquastic Hamiltonians, Perron–Frobenius theorem implies that the ground state is necessarily same-sign in the computational basis. As a result, the admissible subspace dynamically accessible to the ground state remains confined to the same-sign sector. By contrast, introducing a non-stoquastic XX driver opens access to opposite-sign sectors, enlarging the admissible subspace. Within this expanded subspace, *sign-generating quantum interference*—interference that produces negative amplitudes in the computational basis—enables a *smooth evolution path* that bypasses tunneling. This identifies the distinctive quantum mechanism underlying the speedup and explains why no efficient classical analogue is likely to exist.

2 Results

2.1 GIC Graph Instances

We consider a structurally defined family of graphs, referred to as GIC graphs. Each such graph encodes a planted maximum independent set (MIS) together with an extensive collection of competing maximal independent sets. The construction organizes vertices into clique-based blocks, with inter-block couplings chosen to preserve the planted MIS while inducing classical hardness. Each clique-based block corresponds to a dMIC as defined in (17); see Section 3.2 of Supplement.

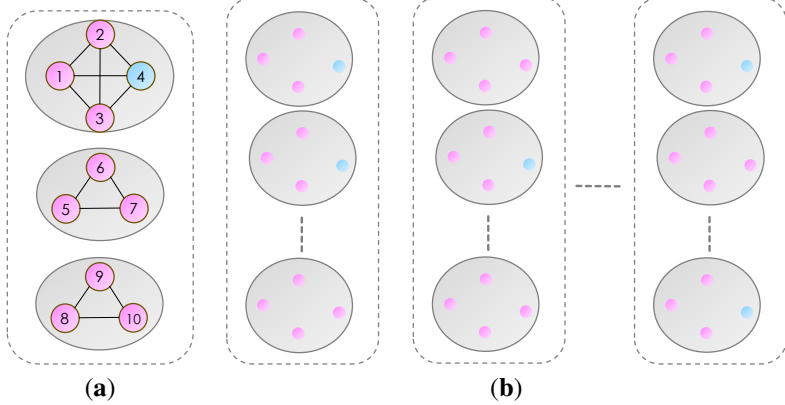


Figure 1: Structure of a dMIC block and a GIC graph. (a) A single dMIC block consisting of three cliques of sizes $(4, 3, 3)$. Each maximal independent set is obtained by selecting exactly one vertex from each clique, yielding $4 \times 3 \times 3$ degenerate maximal independent sets. The highlighted vertex (blue) denotes the planted MIS vertex; all remaining vertices are non-MIS vertices. (b) Schematic structure of a GIC graph composed of multiple blocks. Edges within cliques and between blocks are omitted for clarity. Blocks are initially connected by complete bipartite couplings, after which cross-block edges are selectively removed to embed a unique planted global MIS spanning multiple blocks, while preserving degree-oblivious local structure.

A dMIC of size k consists of k *independent cliques* (i.e., no edges exist between them), denoted as $\text{Clique}(n_i)$, where n_i is the clique size, for $1 \leq i \leq k$. Each maximal independent set within a dMIC is formed by selecting exactly one vertex from each clique. The resulting degeneracy is therefore $\prod_{i=1}^k n_i$. We will refer to each such dMIC as a *dMIC block*. An illustration of a single dMIC block is shown in Fig. 1(A).

A GIC instance consists of at least three such dMIC blocks. A schematic illustration of the full construction is shown in Fig. 1(B). Within each block, vertices belonging to the same clique are fully connected, and different blocks are initially connected via complete bipartite graphs. A unique global MIS is then planted by selecting a fixed number of cliques in each block and choosing one representative vertex per selected clique. All cross-block edges among these representatives are removed, ensuring that the planted set is independent and maximal while necessarily spanning at least three blocks.

To prevent planted MIS vertices from being distinguishable by degree while preserving global optimality, the graph is further modified using an *anchored degree thinning* procedure with global uniqueness protection. Because this procedure depends only on local neighborhood information, it can be implemented efficiently. Overall, the GIC instances considered here are constructible in polynomial time.

Correspondence between dMIC and degenerate local minima. The MIS problem can be encoded in the ground state of the MIS-Ising problem Hamiltonian, as detailed in Section 2 of Supplement. Each maximal independent set corresponds to a local minimum of the problem Hamiltonian. A collection of maximal independent sets all having the same size m corresponds to a set of *degenerate* local minima with equal energy $-m$. Thus, each dMIC induces a set of degenerate local minima (LM)—forming a wide basin—in the MIS-Ising energy landscape. The terms LM and dMIC are thus used interchangeably when no ambiguity arises, with LM used in place of dMIC when emphasizing the corresponding energy landscape structure. We use GM to refer both to the (global) maximum independent set and to its corresponding global minimum in the energy landscape.

Further motivation for the GIC construction and its relation to the structural origin of classical hardness in MIS is discussed in Section 3.2 of Supplement.

Anchored degree thinning. [Move to Supplement.] To prevent planted MIS vertices from being distinguishable by degree while preserving global optimality, we apply an *anchored degree thinning* procedure. For each non-MIS vertex v belonging to a clique that contains a planted MIS vertex m , incident edges are selectively removed so that the post-thinning degree of v is the same as the degree of its anchor m . Edge removals are restricted to neighbors that (i) are not part of the planted MIS, (ii) lie outside the clique of v , and (iii) are neighbors of the anchor m . A local safeguard

Table 1: Classical solver performance on a scaled GIC family. (Top) Description of an example GIC family parametrized by an integer k . Each instance consists of three blocks specified by (m_i, n_i) , $i = 1, 2, 3$, where for each block i , m_i denotes the number of cliques and each clique has size n_i . The planted MIS is specified by parameters (g_1, g_2, g_3) , where g_i denotes the number of MIS vertices in block i (one vertex per selected clique). The planted MIS size is $|\text{MIS}| = g_1 + g_2 + g_3$. (Bottom) Classical solver performance for selected instances from this family. As k increases, ReduMIS transitions from early termination to cutoff-limited success; for the largest instance shown, the time limit was increased from 1200 s to 2400 s to allow recovery of the planted MIS. (Reported ReduMIS runtimes may slightly exceed the nominal cutoff due to solver overhead.) Parallel tempering (PT), run with a fixed 60 s time limit, becomes trapped in suboptimal basins and fails to reach the planted MIS across all instances. All experiments were performed on a local Apple MacBook Pro equipped with an Apple M1 Max processor and 64 GB of memory.

Instance definition (GIC family)					
		(m_1, n_1)	(m_2, n_2)	(m_3, n_3)	(g_1, g_2, g_3)
		$(4 + 4k, 9)$	$(8 + 4k, 6)$	$(3 + 2k, 4)$	$(2 + 2k, 6 + 2k, 2)$

Classical solver performance				
k	$ V $	Planted MIS	ReduMIS runtime / time limit (s)	PT output (time limit = 60 s)
0	96	10	50.2 / 1200	8
3	300	22	414.0 / 1200	20
5	436	30	798.4 / 1200	24
7	572	38	2676.1 / 2400	36

further ensures that the set of removed neighbors does not form an independent set, which guarantees that replacing m by v cannot yield a maximal independent set of equal size, thereby preserving the global uniqueness of the planted MIS. Each vertex is allowed to participate in thinning at most once. After a vertex has been thinned, it is excluded from further thinning operations, including participation as a removable neighbor in subsequent thinning steps. This prevents successive thinning steps from propagating across the graph and ensures that degree reductions do not concatenate to form large independent sets. Because the procedure depends only on local neighborhood information and clique membership, it can be implemented efficiently and does not alter the planted solution.

2.2 Classical Hardness

We evaluate classical performance using the representative algorithm (ReduMIS) from KaMIS (18, 19), a state-of-the-art framework for the maximum independent set problem that combines aggressive graph reductions with evolutionary local search and has been shown to outperform exact solvers on a wide range of benchmark instances. We further include a parallel tempering (PT) baseline (20), which represents a standard stochastic optimization approach that probes the energy landscape directly.

The goal of this evaluation is to establish that leading classical approaches encounter difficulty due to the underlying combinatorial structure of the instances, as expected.

In our experiments, we restrict attention to the simplest nontrivial instances consisting of exactly three dMIC blocks with uniform clique sizes within each block. The description of one example GIC family and the corresponding solver results are presented in Table 1.

2.3 DIC-DAC-DOA on GIC Graphs

The DIC-DAC-DOA algorithm was motivated by turning around the obstacle of stoquastic TFQA—specifically, the presence of an anti-crossing caused by the competition between the energies *associated with* LM and GM. Informally, such an anti-crossing originates from a crossing of the bare energies associated with LM and GM, as illustrated in Figure 2(a–c).

The full algorithm consists of two phases; see Table 2. Phase I uses polynomial-time TFQA to identify an independent-clique (IC) structure associated with the critical LM, which is responsible for the (right-most) anti-crossing with GM in the TFQA ground state evolution. Phase II constructs an XX-driver—based on the identified IC—to remove this anti-crossing. This process is repeated iteratively: at each iteration, the algorithm identifies the next critical

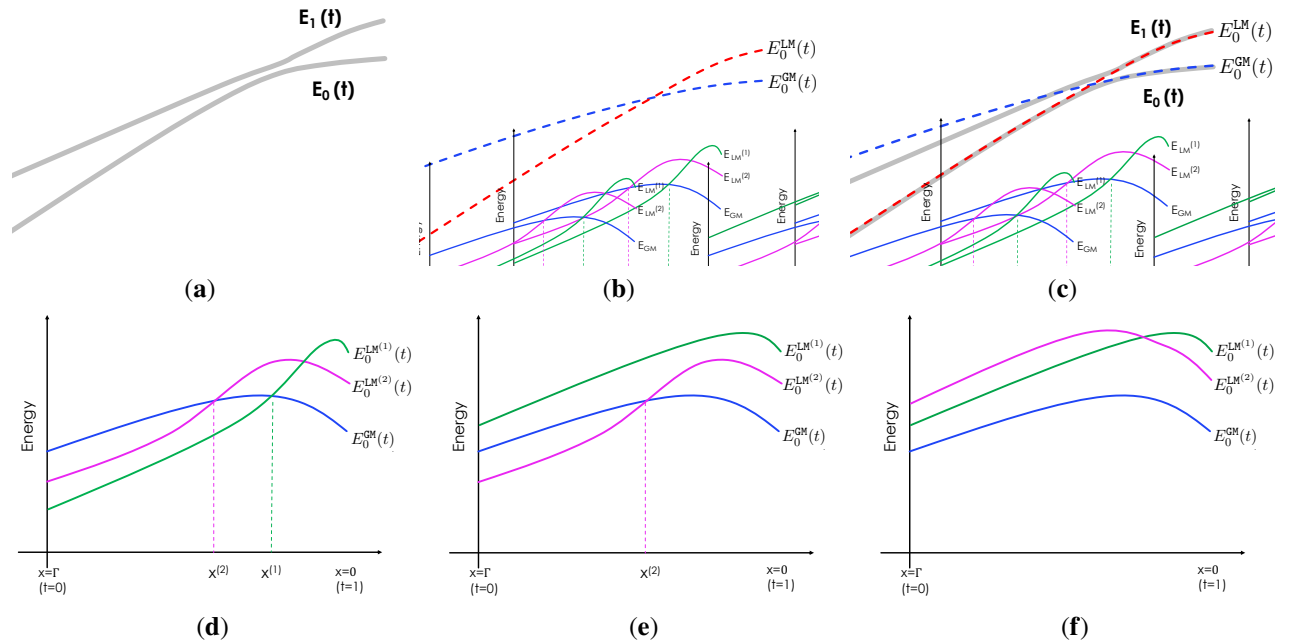


Figure 2: Anti-crossings and their iterative removal by DIC-DAC-DOA. (a–c) **Illustration of an (LM, GM)-anti-crossing.** (a) An anti-crossing between the lowest two levels $E_0(t)$ and $E_1(t)$. (b) Bare energies $E_0^{\text{LM}}(t)$ and $E_0^{\text{GM}}(t)$ cross. (c) Overlay showing that the anti-crossing originates from this bare crossing. (d–f) **Conceptual illustration of the iterative removal of anti-crossings by DIC-DAC-DOA.** (d) Under TFQA, the bare energy $E_0^{\text{GM}}(t)$ (blue) crosses those of two local minima, $E_0^{\text{LM}^{(1)}}(t)$ and $E_0^{\text{LM}^{(2)}}(t)$ at $x^{(1)} = x(t_1)$ and $x^{(2)} = x(t_2)$. Each such bare crossing corresponds to an $(\text{LM}^{(i)}, \text{GM})$ -anti-crossing in the system spectrum. (e) After the first iteration of DIC-DAC-DOA, the first crossing is removed by lifting $E_0^{\text{LM}^{(1)}}(t)$, while the second remains. (f) A second iteration applies the same procedure to lift $E_0^{\text{LM}^{(2)}}(t)$, completing the removal of both anti-crossings.

LM, constructs an additional driver term, added to the system Hamiltonian. In this way, the algorithm progressively removes small-gap obstructions from the system, as illustrated conceptually in Figure 2(d–f). Within this framework, the presence of an anti-crossing corresponds to exponentially slow adiabatic evolution, whereas its removal leads to polynomial-time performance.

Table 2: Algorithm overview of the full DIC-DAC-DOA algorithm.

Phase I: Independent-cliques extraction via polynomial-time TFQA.

1. Run TFQA with system Hamiltonian $H(t) = x(t)H_X + p(t)H_{\text{problem}}$ using a polynomial annealing time to return the excited states involved in the anti-crossing.
2. Extract a set of seeds (local-minima states) from the TFQA output.
3. Apply a classical post-processing procedure to identify an independent-cliques (IC) structure from these seeds.

Phase II: Non-stoquastic annealing with an XX-driver.

1. Construct an XX-driver graph G_{driver} from the IC structure identified in Phase I.
2. Define a new time-dependent Hamiltonian $H(t) = x(t)H_X + j_{\text{XX}}(t)H_{\text{XX}} + p(t)H_{\text{problem}}$.
3. For each feasible coupling strength J_{XX} , evolve the system using a three-stage schedule:
 - **Stage 0:** initialization;
 - **Stage 1:** energy-guided localization;
 - **Stage 2:** interference-driven transition.
4. Measure the final state to extract the optimal solution.

First, we recall the system Hamiltonian for DIC-DAC-DOA:

$$H(t) = x(t)H_X + j_{\text{XX}}(t)H_{\text{XX}} + p(t)H_{\text{problem}},$$

where $H_X = -\sum_i \sigma_i^x$, $H_{\text{XX}} = \sum_{(i,j) \in E(G_{\text{driver}})} \sigma_i^x \sigma_j^x$, and H_{problem} is the MIS-Ising Hamiltonian defined as

$$H_{\text{problem}} = \sum_{i \in V(G)} (-w_i) \tilde{\sigma}_i^z + J_{\text{zz}}^{\text{clique}} \sum_{(i,j) \in E(G_{\text{driver}})} \tilde{\sigma}_i^z \tilde{\sigma}_j^z + J_{\text{zz}} \sum_{(i,j) \in E(G) \setminus E(G_{\text{driver}})} \tilde{\sigma}_i^z \tilde{\sigma}_j^z. \quad (1)$$

Here $\tilde{\sigma}_i^z := \frac{I + \sigma_i^z}{2}$, where the coupling $J_{\text{zz}}^{\text{clique}}$ is assigned to edges corresponding to cliques in the driver graph, while J_{zz} is assigned to all remaining edges. The value of $J_{\text{zz}}^{\text{clique}}$ is set sufficiently large to restrict the system to the clique low-energy subspace, effectively cutting off the high-energy sector, similar to the idea of the Projection Lemma in (21). The time-dependent parameter schedule $j_{\text{XX}}(t)$ depends on the XX-coupling strength J_{XX} . In particular, $j_{\text{XX}}(t) \equiv 0$ when $J_{\text{XX}} = 0$, so this case reduces to TFQA without the XX-driver. The system Hamiltonian is stoquastic in the computational basis for $J_{\text{XX}} \leq 0$, and non-stoquastic for $J_{\text{XX}} > 0$.

We now summarize how the resulting non-stoquastic evolution modifies the adiabatic path; a detailed analysis is given in Methods. The adiabatic evolution proceeds through three stages.

Stage 0: High-energy clique configurations are adiabatically suppressed, allowing restriction to a low-energy effective Hamiltonian.

Stage 1: The evolution is smoothly steered toward the GM-support region without encountering an anti-crossing.

Stage 2: The original anti-crossing is removed through a see-saw spectral reshaping, enabling a smooth adiabatic path that can be explained through sign-generating quantum interference.

3 Discussion

In this work, we identify a structurally defined family of MIS instances, referred to as GIC graphs, that are classically hard due to the presence of extensive competing local minima organized by independent-cliques substructures. For these instances, we design and analyze a non-stoquastic adiabatic quantum optimization algorithm that augments TFQA with a tailored XX-driver. The algorithm reshapes the low-energy spectrum and removes the small-gap anti-crossings that arise in stoquastic evolution as a consequence of tunneling, yielding a polynomial-time adiabatic path on GIC instances where both TFQA and state-of-the-art classical algorithms exhibit exponential difficulty. The essential quantum mechanism enabling the speedup is the use of a non-stoquastic XX-driver to access an enlarged, sign-structured admissible subspace beyond the stoquastic regime.

More specifically, our analysis identifies two key mechanisms responsible for enabling the smooth evolution path:

- **Structural steering:** energy-guided localization within the same-sign block that steers the ground state smoothly into the GM-supporting region, bypassing tunneling-induced anti-crossings.
- **Sign-generating quantum interference:** production of negative amplitudes that enables an opposite-sign path through destructive interference in the computational basis.

The analysis of these mechanisms is supported by both analytical derivations and numerical validation, and can, in principle, be made rigorous with further work.

Quantumness and Absence of Classical Analogues

The emergence of negative amplitudes—produced by sign-generating interference due to the non-stoquastic Hamiltonian—serves as a witness to the quantum nature of the speedup. Classical simulation algorithms, such as quantum Monte Carlo methods (see (22) and references therein), rely on the non-negativity of wavefunctions in the computational basis and break down in regimes where interference induces sign structure. This places the algorithm beyond the reach of (eventually) stoquastic annealing and efficient classical simulation.

From the perspective of classical solvers, the effect of sign-generating interference may be hard to reproduce classically. Algorithmically speaking, the XX-driver with appropriately tuned coupling strength J_{xx} enables a form of collective suppression of local minima, induced by edge couplings that effectively reduce vertex weights—while selectively preserving the global minimum, even in the presence of partial overlap. To the best of our understanding, no known classical algorithm is able to replicate this effect, which appears to be a genuinely quantum capability.

Together, these points position Dic-Dac-Doa as a candidate for demonstrating quantum advantage, providing an explicit example of the emphasis expressed in recent surveys of the field (23), where the origin of the advantage can be traced to a specific quantum mechanism.

Relaxing the Structured Input Assumption

Our analysis is developed under the structured GIC assumption: each critical degenerate local minima—corresponding to a set of maximal independent sets of fixed size—is formed by a set of *independent cliques* (dMIC). This assumption underlies both the design of the XX-driver and the block decomposition of the Hamiltonian. The independence of cliques is assumed primarily to allow efficient identification during Phase I. In principle, one can allow the cliques to be dependent (dMDC), meaning that some edges are permitted between cliques. In this case, the cliques may need to be identified heuristically rather than exactly. Under suitable conditions, the algorithm may remain robust even when applied to dMDC structures. More generally, each critical degenerate local minima in the real-world application may consist of a set of disjoint dMDCs. A clique-based driver graph may still be constructed in such cases, but the generalization becomes more intricate and may require further algorithmic refinements. Other future directions include the study of weighted MIS instances and adaptive strategies for selecting or optimizing J_{xx} during the anneal.

Our work thus aligns with the articulation that “the most important reason to seek knowledge of instances with a quantum speedup is because an understanding of the type of structure that leads to advantage can help to find real-world problems where the advantage persists” (2). In this sense, the identification of structured MIS instances together with the associated quantum mechanism in Dic-Dac-Doa offers a concrete instantiation of two central stages (Stage II and III) emphasized in (2).

From an algorithmic standpoint, AQC offers a physics-driven framework for optimization. By explicitly incorporating problem structure into the design of the system Hamiltonian and by analyzing the resulting spectral behavior

through the presence or absence of anti-crossings, we demonstrate how AQC can be used as a principled algorithm design paradigm rather than a black-box heuristic. This approach leverages well-established tools from mathematical physics, including perturbative analysis, effective Hamiltonian theory, and angular momentum methods, in combination with algorithmic and graph-theoretic insights.

There are challenges in realizing the proposed non-stoquastic algorithm directly on quantum annealing hardware, including constraints related to hardware architecture, the minor-embedding problem (7, 8), and the requirements of error correction, as also noted in (15). Indeed, digitized AQC was promoted there as “a viable quantum algorithm for execution on an error-corrected digital quantum device.” Direct Trotterization-based digitized implementations, however, may not be resource-optimal. Instead, one may adopt a QAOA-like approach (24) to digitize the Dic-DAC-DoA algorithm, which can provide a more practical route forward.

Even prior to an immediate real-world application, our results are already valuable. In particular, our analysis produces scalable small-scale models, derived from our structural reduction, that capture the essential dynamics of the algorithm. These reduced models preserve the relevant block structure and interference mechanisms while dramatically decreasing the effective system size, with each large clique contracted to a single effective vertex. As a result, the reduced instances are sufficiently small to be accessible on current and near-term gate-model quantum processors through digitized AQC, using Trotterized implementations. This makes them well suited for validating hardware progress and for experimental verification of the quantum advantage mechanism.

4 Methods

The goal of the algorithm is to remove anti-crossings one by one using an XX-driver with appropriate choices of J_{XX} . Detailed derivations, proofs, and numerical confirmations are provided in Supplement.

We analyze how a single anti-crossing is encountered and removed. As explained above, such an anti-crossing involves a critical LM and the global minimum (GM). The LM corresponds to a degenerate set of maximal independent sets generated by the cliques forming a dMIC, which are identified in Phase I and used to construct the XX-driver. We then restrict attention to reduced bipartite substructures formed by the LM and GM.

4.1 Phase I: Identification of the LM-associated clique structure

In Phase I, a polynomial-time transverse-field quantum annealing (TFQA) procedure is used to identify the clique structure associated with a critical LM. Specifically, TFQA is run with the stoquastic Hamiltonian $H(t) = x(t)H_X + p(t)H_{\text{problem}}$ for a polynomial annealing time, and the resulting measurement outcomes are recorded.

As shown in (25) (see Section 11 of Supplement for details), an (LM,GM)-anti-crossing under TFQA exhibits an exponentially small gap. As a consequence, polynomial-time TFQA undergoes a diabatic transition at the anti-crossing and transitions into configurations associated with LM. The resulting output thus provides a collection of seed configurations associated with LM.

Under the structural assumption that the cliques forming the dMIC are mutually independent, the underlying cliques structure can be identified efficiently by a classical post-processing step. The set of recovered cliques is then used to construct the XX-driver graph for Phase II of the algorithm. Thus, in what follows, LM, dMIC, and the associated XX-driver refer to the same independent-cliques substructure. The Phase I mechanism is schematically illustrated in Fig. 3.

4.2 Bipartite substructures: G_{dis} and G_{share}

To analyze the competition between a critical LM and the GM, we consider two canonical bipartite substructures.

- G_{dis} (disjoint-structure), in which the vertex sets supporting the LM and the GM are disjoint.
- G_{share} (shared-structure), in which the GM shares exactly one vertex with each clique comprising the LM.

We first define the *disjoint-structure graph* $G_{\text{dis}} = (V, E)$, in which the vertex set is partitioned into left and right components with the following properties:

- The left component consists of a set $L = \{C_1, \dots, C_{m_L}\}$ of m_L disjoint cliques, each $C_i = \text{Clique}(w_i, n_i)$, with vertex set $V_L = \bigcup_{i=1}^{m_L} C_i$.

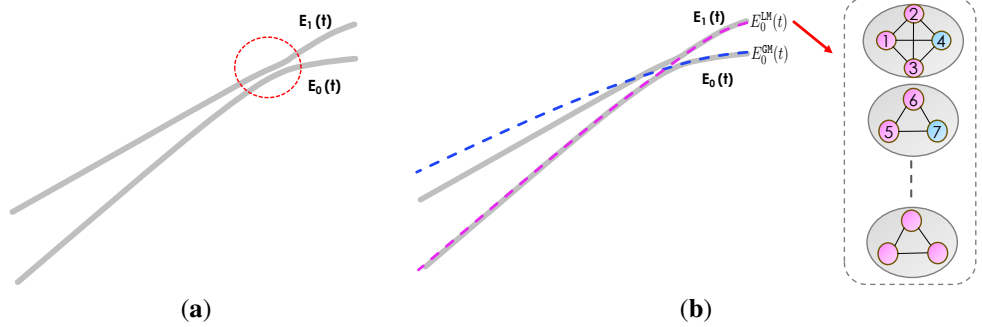


Figure 3: Schematic illustration of Phase I. (a) An anti-crossing between the lowest two energy levels under stoquastic TFQA. (b) The anti-crossing originates from competition between the energies associated with LM and GM; the LM corresponds to a degenerate set of maximal independent sets generated by cliques forming a dMIC.

- The right component R consists of m_r independent vertices, each with weight w_r .
- Every vertex in V_L is adjacent to every vertex in R .

Throughout this work we focus on the unweighted MIS case and assume uniform weights $w_i = w_r = 1$. In the MIS–Ising energy landscape defined by H_{problem} , the left component V_L induces a degenerate set of local minima LM with degeneracy $\prod_{i=1}^{m_l} n_i$ and energy $-m_l$, while the right component R defines the global minimum GM of size $m_g = m_r$ and energy $-m_g$.

The *shared-structure graph* G_{share} differs from G_{dis} in that each vertex in R is adjacent to all but one vertex in each clique of L . This modification allows the GM to include exactly one shared vertex from each clique in L , thereby introducing overlap between LM and GM. The GM then consists of these shared vertices together with all vertices in R , yielding total size $m_g = m_l + m_r$. The structures of G_{dis} and G_{share} are illustrated in Figure 4.

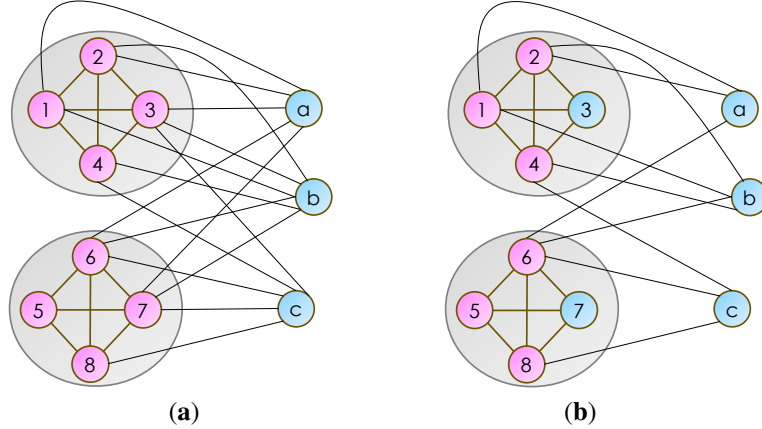


Figure 4: Example graphs illustrating the G_{dis} and G_{share} structures. Recall that each LM here is structurally a dMIC. (a) Disjoint-structure graph G_{dis} : The set L consists of $m_l = 2$ disjoint cliques, each of size $n_1 = n_2 = 4$, whose vertices (pink) generate the local minima LM. The set R (blue) consists of $m_r = 3$ independent vertices forming the global minimum GM. (a) Shared-structure graph G_{share} : Relative to G_{dis} , two vertices in L are shared between the LM and GM, and are therefore shown in blue instead of pink. The global minimum (in blue) has $m_g = 5$ vertices. In both cases, edges between the pink vertices in L and all vertices in R are complete, though not all are shown for visual clarity.

For convenience, we write $m := m_l$ when no ambiguity arises. We assume $\sum_{i=1}^m \sqrt{n_i} > m_g$, which ensures that the competition between LM and GM induces an anti-crossing under stoquastic annealing.

We focus our Phase II analysis on the shared-structure case G_{share} , which captures the worst-case structure required for the full analysis. The disjoint-structure case G_{dis} is included both to illustrate the underlying mechanism of Dic-Dac-Doa—since the corresponding blocks of the effective Hamiltonian are decoupled and the analysis reduces to the

same-sign block—and because it represents the worst-case structure for the analysis of anti-crossing gap under TFQA, as detailed in Section 11 of Supplement.

4.3 Overview: Three-Stage Adiabatic Schedule in Phase II

In Phase II, the DIC-DAC-DOA Hamiltonian is decomposed into three stages, distinguished by the relative ordering of the transverse-field strengths $\Gamma_0 > \Gamma_1 > \Gamma_2$ and by when the problem and driver couplings are activated, as illustrated by the annealing schedule in Fig. 5.

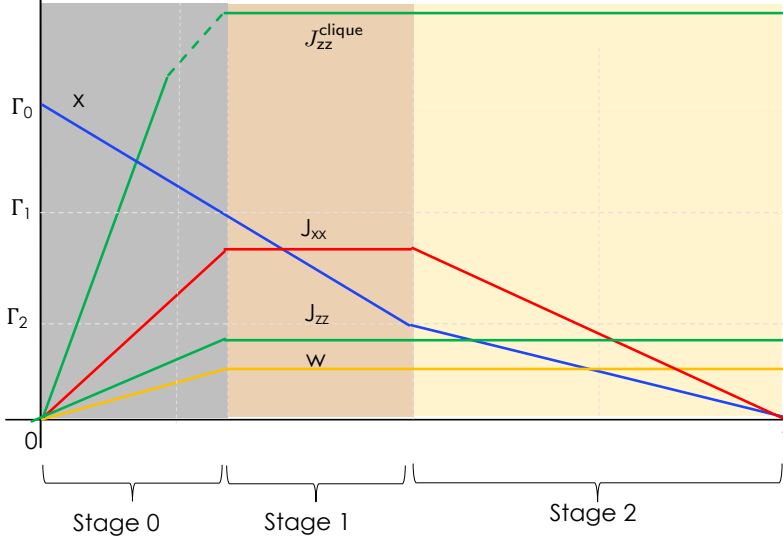


Figure 5: Annealing parameter schedule for the system Hamiltonian $H(t) = x(t)H_x + j_{xx}(t)H_{xx} + p(t)H_{\text{problem}}$. The transverse field $x(t)$ (blue) begins at Γ_0 , decreases to Γ_1 in Stage 0, then to Γ_2 in Stage 1, and reaches 0 at the end of Stage 2. The XX-coupling strength $j_{xx}(t)$ (red) increases linearly to J_{xx} in Stage 0, remains constant in Stage 1, and decreases to 0 in Stage 2. Vertex weights w_i (orange) and ZZ-couplings J_{zz} , J_{zz}^{clique} (green) ramp to their final values in Stage 0 and remain fixed thereafter.

This decomposition is conceptual and reflects the qualitative structure of the evolution; technical details are provided in the subsequent sections and in Supplement.

Stage 0 (Low-energy subspace formation). At early times, high-energy configurations containing intra-clique violations are adiabatically suppressed. As a result, the dynamics become effectively restricted to the clique low-energy sector associated with the identified independent-clique structure. This stage establishes an effective Hamiltonian that governs the subsequent evolution.

Stage 1 (Approach without anti-crossing). Within the resulting low-energy effective Hamiltonian, the system evolves toward the GM-support region while avoiding localization regimes associated with local minima. In this stage, the evolution does not encounter an anti-crossing, ensuring that the system reaches the parameter regime where the non-stoquastic effects become operative.

Stage 2 (Anti-crossing removal). In the final stage, the remaining low-energy competition between LM and GM is resolved. The XX-coupling induces a see-saw reshaping of the spectrum, lifting same-sign local minima while allowing opposite-sign sectors to participate in the evolution. The resulting adiabatic path remains smooth and can be understood in terms of sign-generating quantum interference.

We now analyze each stage in turn, beginning with the construction of the effective low-energy Hamiltonian in Stage 0.

4.4 Stage 0: Effective Low-Energy Hamiltonian

During Stage 0, a large energy penalty J_{zz}^{clique} is applied to the intra-clique edges, where the cliques are those that constitute the XX-driver graph. This separates the Hilbert space into a low-energy sector, consisting of configurations that respect the clique constraints, and a high-energy sector containing states that incur intra-clique energy penalties.

With respect to this decomposition, the system Hamiltonian admits a block form,

$$H = \begin{pmatrix} H^{\text{low}} & V \\ V^\dagger & H^{\text{high}} \end{pmatrix},$$

where H^{low} and H^{high} denote the projections onto the low-energy and high-energy sectors, respectively.

As a result, the evolution at the end of Stage 0 is governed by an effective low-energy Hamiltonian $H_1^{\text{eff}} = H^{\text{low}}$. A detailed derivation of this effective Hamiltonian, together with a proof that the spectral gap remains large throughout Stage 0, is provided in Section 8 of Supplement. From this point onward, all block decompositions and dynamical analyses refer to the time-dependent effective Hamiltonian H_1^{eff} governing Stages 1 and 2.

4.5 Angular-momentum block decomposition and J_{xx} -induced energy reshaping

We develop a block decomposition of the effective Hamiltonian into same-sign and opposite-sign sectors in the angular-momentum basis induced by the cliques in the XX-driver graph.

Within this basis, the XX-coupling term acts diagonally. In particular, the coupling strength J_{xx} shifts the energies of same-sign and opposite-sign blocks with opposite signs. This reshapes the spectrum in a see-saw fashion: increasing J_{xx} raises the energies associated with LM in the same-sign block while lowering those of the opposite-sign blocks. With an appropriate choice of J_{xx} , this energy reshaping removes the (LM, GM)-anti-crossing under stoquastic evolution.

In the following, we first analyze the angular-momentum structure and J_{xx} -induced energy reshaping for a single clique, and then extend the analysis to a collection of independent cliques (a dMIC bare subsystem) and finally to the full effective Hamiltonian.

4.5.1 Single-clique analysis

Let \mathcal{L}^{ind} denote the low-energy subspace of a single clique, $\text{Clique}(w_c, n_c)$, where $w_c \equiv 1$ denotes the vertex weight and n_c the clique size. The low-energy subspace \mathcal{L}^{ind} , which consists of the $n_c + 1$ independent-set configurations of the clique, admits a natural decomposition in the total angular-momentum basis into a single effective spin- $\frac{1}{2}$ (same-sign) sector and a collection of spin-0 (opposite-sign) sectors:

$$\mathcal{L}^{\text{ind}} = \left[\frac{1}{2} \right]_{n_c} \oplus \underbrace{0 \oplus \cdots \oplus 0}_{n_c - 1}. \quad (2)$$

The spin- $\frac{1}{2}$ sector consists of two same-sign basis states, while each spin-0 sector consists of a single opposite-sign basis state.

An illustration of this basis transformation is shown in Figure 6(a,b).

The effective Hamiltonian on the spin- $\frac{1}{2}$ (same-sign) sector is a 2×2 matrix of the form

$$B(w_c^{\text{eff}}, \sqrt{n_c} \mathbf{x}) = \begin{bmatrix} -\left(w_c - \frac{n_c - 1}{4} \mathbf{j} \mathbf{x} \mathbf{x}\right) & -\frac{\sqrt{n_c}}{2} \mathbf{x} \\ -\frac{\sqrt{n_c}}{2} \mathbf{x} & 0 \end{bmatrix}$$

with $w_c^{\text{eff}} = w_c - \frac{n_c - 1}{4} \mathbf{j} \mathbf{x} \mathbf{x}$, while each spin-0 (opposite-sign) sector contributes a single eigenvalue $-(w_c + \frac{1}{4} \mathbf{j} \mathbf{x} \mathbf{x})$.

Notice that the XX-coupling $\mathbf{j} \mathbf{x} \mathbf{x}$ is diagonal and acts with opposite sign on the two sectors. It reshapes the spectrum in a see-saw fashion: the same-sign sector is lifted in energy (and its slope magnitude is reduced), while the opposite-sign sectors are lowered. See Figure 7(a).

Moreover, this angular-momentum decomposition can be expressed in terms of coupled subcliques, as illustrated in Figure 6(c), which allows treating non-uniform ZZ-couplings to external vertices and is essential for the global block decomposition of graphs with shared structure.

The details are provided in Section 6 of Supplement.

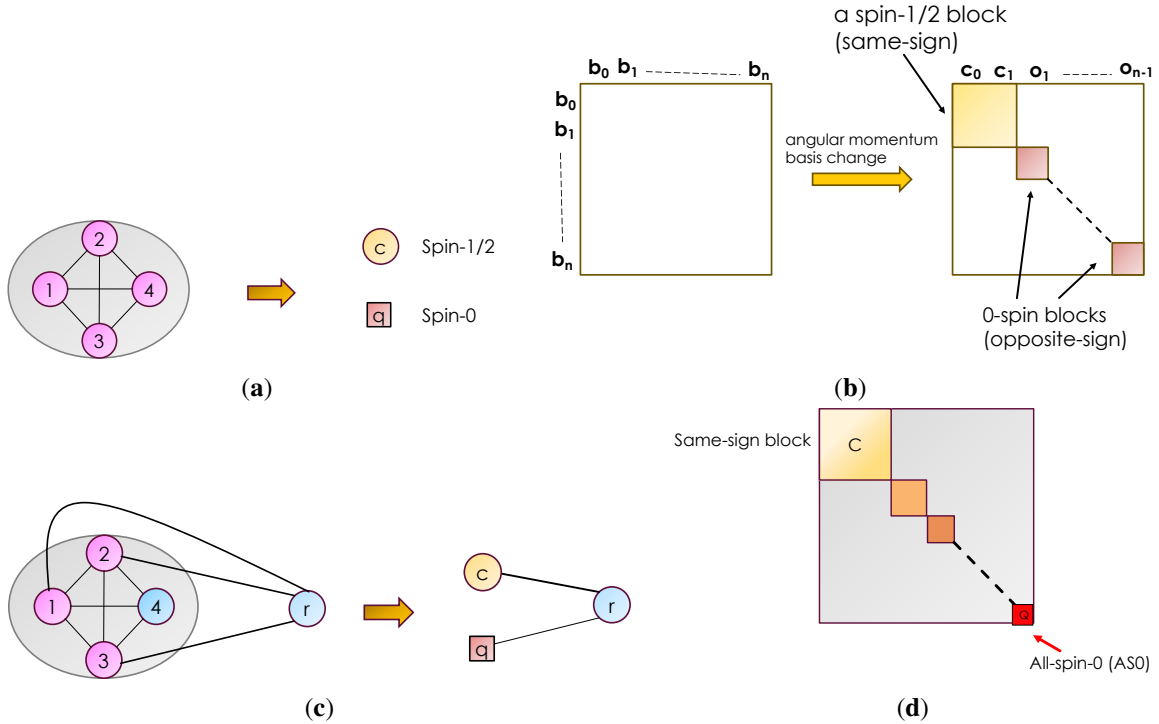


Figure 6: Block decomposition in angular momemtum basis. (a) A clique $\{1, 2, 3, 4\}$ is transformed into an effective spin- $\frac{1}{2}$ component labeled c (orange) and a representative spin-0 component labeled q (red square). (b) **Single clique.** The low-energy product basis decomposes into an effective spin- $\frac{1}{2}$ same-sign block and $n - 1$ spin-0 opposite-sign blocks in the angular-momentum basis. (c) Partial adjacency of an external vertex r to a clique leads to ZZ-couplings to both the same-sign and opposite-sign sectors, inducing mixing between them. (d) **Full system.** Tensoring the single-clique structure yields a block decomposition of the effective Hamiltonian H_1^{eff} into a dominant same-sign block H_C and opposite-sign blocks, including the AS0 block H_Q ; these blocks are decoupled in G_{dis} and coupled via $H_{\text{inter-block}}$ in G_{share} .

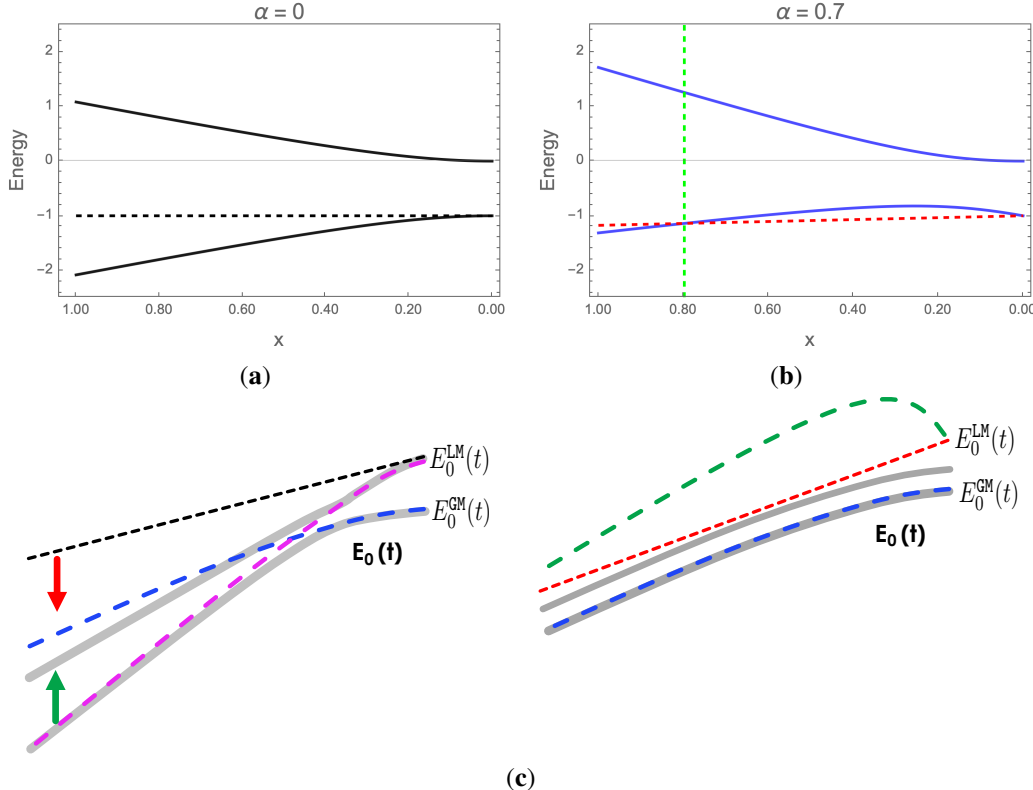


Figure 7: See-saw reshaping of the spectrum induced by J_{xx} . (a–b) Effect of the XX-coupling strength J_{xx} on the low-energy spectrum of a single clique, with $J_{xx} = \alpha\Gamma_2$. The transverse field x decreases from $\Gamma_2 = 1$ to 0, with $j_{xx} = \alpha x$. **See-saw effect:** increasing J_{xx} raises the energies of the same-sign sector (black to blue) while lowering the energy of the opposite-sign sector (black dashed to red dashed). (c) Schematic illustration of the resulting see-saw mechanism in the full system: for $J_{xx} = 0$, an (LM, GM)-anti-crossing appears under stoquastic TFQA, while for a feasible nonzero J_{xx} , the same-sign LM energy is lifted (pink dashed to green dashed) and the lowest opposite-sign energy is lowered (black dotted to red dotted), removing the anti-crossing.

4.5.2 Bare subsystem analysis

We now extend the single-clique analysis to a collection of independent cliques (a dMIC), which together forms a *bare subsystem*. It is a *subsystem* because we consider only the subgraph induced by the dMIC, and it is *bare* because it is fully decoupled from the rest of the graph. Note that either LM or GM by itself forms a bare subsystem, where each clique in GM has size one.

Consider the bare subsystem formed by m independent cliques $\text{Clique}(w_i, n_i)$, where $w_i \equiv 1$ denotes the vertex weight and n_i the size of the i th clique.

The low-energy space of the bare subsystem decomposes into three classes of sectors: the *same-sign sector* C^{bare} , the *intermediate opposite-sign sectors* W^{bare} , and the *all-spin-zero (AS0) opposite-sign sector* Q^{bare} .

From the single-clique result (Eq. (2)), the low-energy subspace of each clique decomposes as:

$$\mathcal{L}_i = \left[\frac{1}{2} \right]_{n_i} \oplus \underbrace{0 \oplus \cdots \oplus 0}_{n_i-1}.$$

Hence, the total low-energy subspace \mathcal{L} of the bare subsystem is given by:

$$\mathcal{L} = \bigotimes_{i=1}^m \mathcal{L}_i = \bigotimes_{i=1}^m \left(\left[\frac{1}{2} \right]_{n_i} \oplus \underbrace{0 \oplus \cdots \oplus 0}_{n_i-1} \right) = \bigoplus \left(\bigotimes_{i=1}^m \left[\frac{1}{2} \text{ or } 0 \right] \right),$$

where the direct sum ranges over all tensor products selecting one spin- $\frac{1}{2}$ and $n_i - 1$ spin-zeros from each clique.

This decomposition yields $\prod_{i=1}^m n_i$ block subspaces. Among them, the block

$$C^{\text{bare}} := \bigotimes_{i=1}^m \left[\frac{1}{2} \right]_{n_i}$$

is composed entirely of spin- $\frac{1}{2}$ factors and is referred to as the *same-sign sector*.

At the opposite extreme, there are $\prod_{i=1}^m (n_i - 1)$ blocks composed entirely of spin-0 factors:

$$Q^{\text{bare}} := \bigotimes_{i=1}^m 0,$$

referred to as the *all-spin-zero (AS0) opposite-sign sector*.

The remaining opposite-sign blocks, each containing a mixture of spin- $\frac{1}{2}$ and spin-0 components, are called the *intermediate sectors*. Let W^{bare} denote one such intermediate sector.

With this sector decomposition, projecting the effective Hamiltonian yields a block-diagonal structure.

In particular, the restriction to the same-sign sector takes the form

$$H_{C^{\text{bare}}} = \sum_{i=1}^m B_i(w_i^{\text{eff}}, \sqrt{n_i} x),$$

where each B_i acts nontrivially only on the i th clique and $w_i^{\text{eff}} = w_i - \frac{n_i-1}{4} j x x$.

The AS0 opposite-sign sector contributes a single energy level,

$$H_{Q^{\text{bare}}} = - \sum_{i=1}^m \left(w_i + \frac{1}{4} j x x \right),$$

while each intermediate opposite-sign sector corresponds to a reduced same-sign block involving fewer active B_i terms, together with an additive energy shift.

Therefore, the bare subsystem has a collective J_{xx} -induced see-saw reshaping of its spectrum, directly as a sum of single-clique contributions. Furthermore, the closed-form solutions of the energies (in particular, $E_0^{\text{LM}}(t)$ and $E_0^{\text{GM}}(t)$) enable the derivation of analytic bounds on J_{xx} required to remove the (LM, GM)-anti-crossing.

The details are provided in Section 7 of Supplement.

4.5.3 Block decomposition of the effective Hamiltonian

Finally, we assemble the full effective Hamiltonian by combining the L bare-subsystem structure with the remaining degrees of freedom in R . The same-sign sector of the full system is defined as

$$C = C^{\text{bare}} \otimes \left(\mathbb{C}^2\right)^{\otimes m_r},$$

where $m_r = |R|$. Similarly, the opposite-sign sectors of the full system are given by

$$\mathcal{W} = \mathcal{W}^{\text{bare}} \otimes \left(\mathbb{C}^2\right)^{\otimes m_r}, \quad Q = Q^{\text{bare}} \otimes \left(\mathbb{C}^2\right)^{\otimes m_r}.$$

Accordingly, Q is also referred to as the all-spin-zero (AS0) opposite-sign sector of the full system.

With these definitions, the effective Hamiltonian decomposes into a same-sign block H_C and multiple opposite-sign blocks H_W and H_Q , which are either decoupled (in the disjoint-structure case) or coupled (in the shared-structure case), as illustrated schematically in Figure 6(d).

The explicit block Hamiltonians, coefficients, and inter-block couplings are derived in Section 9.1 of Supplement.

The initial ground state resides in the same-sign block H_C at the beginning of Stage 1.

4.6 Main Analysis: Two-Stage Evolution and Feasible Bounds on J_{xx}

The main idea of the analysis is to exploit the J_{xx} -induced see-saw reshaping of the signed block spectrum, to remove the original (LM,GM)-anti-crossing. While increasing J_{xx} lifts the energies associated with LM in the same-sign block, it simultaneously lowers those of the opposite-sign blocks, introducing a trade-off that constrains the allowable range of J_{xx} . If J_{xx} is too small, the local minima in the same-sign block are not lifted sufficiently to remove the anti-crossing. If J_{xx} is too large, the opposite-sign blocks are lowered too far, leading to new anti-crossings. As a result, the success of the algorithm depends critically on choosing J_{xx} within an appropriate window.

We divide the evolution into two stages: Stage 1 and Stage 2. Stage 2 addresses the original (LM,GM)-anti-crossing and removes it via the see-saw effect; see Figure 7(c) for an illustration. Stage 1 ensures that the ground state evolves smoothly into the GM-support region—which serves as the starting point for Stage 2—without encountering a new anti-crossing. In terms of parameters, the XX-coupling strength remains fixed at J_{xx} throughout Stage 1 and is reduced to zero during Stage 2.

We now briefly summarize the role of J_{xx} bounds and how they jointly ensure a smooth two-stage evolution. The Stage-Separation bound J_{xx}^{sep} together with a J_{zz} bound ensure that Stage 1 is effectively confined to the same-sign block, allowing Stage 1 and Stage 2 to be analyzed separately; the Lifting bound J_{xx}^{lift} ensures the original anti-crossing is removed; the Steering bound J_{xx}^{steer} directs the system smoothly into the R -localized region (bypassing tunneling) during Stage 1, and Stage 2 is secured by the Sinking bound J_{xx}^{sink} , which prevents the emergence of a new anti-crossing when the lowest opposite-sign block participates. The four analytical feasibility bounds on J_{xx} are summarized in Table 2 in Section 9.3 of Supplement.

The resulting evolution can be understood in terms of two key mechanisms: (i) *structural steering* in Stage 1, which guides the evolving ground state away from the LM-supporting region and directly into the GM-supporting region; and (ii) *sign-generating quantum interference* in Stage 2, which enables smooth adiabatic evolution to GM via an opposite-sign path.

4.6.1 Stage 1: Smooth Steering into the GM-Support Region

The purpose of Stage 1 is to steer the ground state smoothly into the GM-support region through *structural steering*, which then serves as the initial condition for Stage 2, without encountering an anti-crossing. Throughout this stage, the dynamics remains confined to the same-sign block, ensured by the Stage-Separation bound J_{xx}^{sep} , together with the requirement $J_{zz} \leq J_{zz}^{\text{inter}}$ in the shared-structure case.

The structural steering mechanism can be understood through two equivalent inner decompositions of the same-sign block: the *L-inner* and the *R-inner* ordering of basis states (Fig. 8). Based on the inner decompositions, we can then describe the two different localizations. If the evolution follows the *R-inner* (*L-inner*, resp.) decomposition, the instantaneous ground state localizes within the lowest-energy R -blocks, which we refer to as *R-localization* (*L-localization*, resp.).

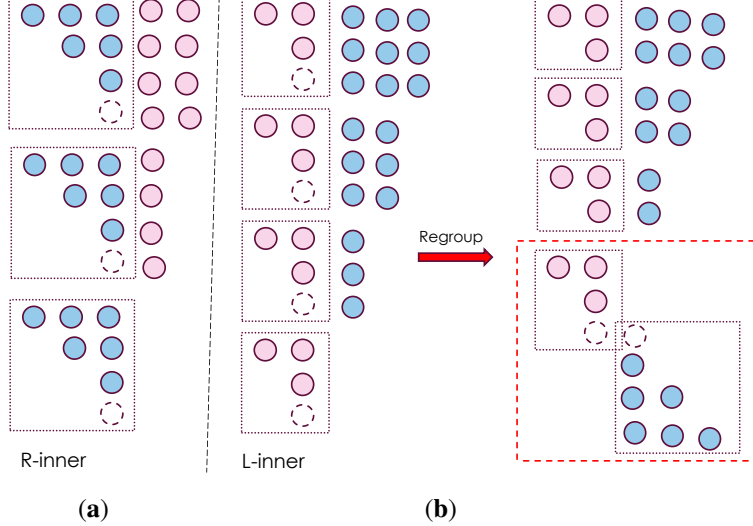


Figure 8: Two equivalent inner orderings of the basis states of the same-sign block (symmetric subspace). Illustrated for $m = 2$, $m_r = 3$. (a) *R-inner* ordering, in which basis states are grouped by the spin-up count in the L subsystem (pink), with each group forming a block over the R subsystem (blue). The dashed circle marks the empty-set basis state. For appropriately large J_{xx} , the adiabatic evolution follows the *R-inner* decomposition, leading to *R*-localization. (b) *L-inner* ordering, obtained by a permutation of basis states, in which basis states are grouped by the spin-up count in the R subsystem. For $J_{xx} = 0$, the evolution follows the *L-inner* decomposition, leading to *L*-localization. The red dashed box highlights the core Hamiltonian H_{core} , corresponding to the reduced two-block structure resulting from *L*-localization.

In the TFQA case (i.e. $J_{xx} = 0$), the evolution follows the *L-inner* decomposition, leading to *L*-localization first. The dynamics reduces to the two-block Hamiltonian H_{core} , where the subsequent tunneling transition from *L*-localized to *R*-localized configurations proceeds through an (L, R) -anti-crossing, as analyzed in Section 11 of Supplement.

However, if J_{xx} is appropriately large, the adiabatic evolution follows the *R-inner* decomposition, leading to *R*-localization, without tunneling. Formally, the smooth *R*-localization is guaranteed by two feasibility bounds: the Lifting bound J_{xx}^{lift} , which forces the ground state toward the lowest *R*-blocks; and the Steering bound J_{xx}^{steer} , which ensures that this localization proceeds smoothly. This analytically established behavior is further confirmed by numerical evidence provided in Section 9.3.2 of Supplement.

4.6.2 Stage 2: Smooth Evolution to GM via an Opposite-Sign Path

The purpose of Stage 2 is to remove the original (LM, GM) -anti-crossing and complete the evolution to the global minimum (GM) without a new anti-crossing, starting from the *R*-localized region prepared at the end of Stage 1. This is achieved by exploiting the see-saw reshaping of the spectrum induced by the XX-coupling, together with quantum interference between opposite sign sectors.

The value of J_{xx} at the start of Stage 2 is chosen sufficiently large, as ensured by the Lifting bound J_{xx}^{lift} , so that the original anti-crossing is removed. In the disjoint-structure graph G_{dis} , the blocks are decoupled, the evolution during Stage 2 remains entirely within the same-sign block. Thus there is no anti-crossing in this case.

In the shared-structure graph G_{share} , the lowest opposite-sign block (the AS0 block) enters the low-energy spectrum during Stage 2. The Sinking upper bound $J_{xx} \leq J_{xx}^{\text{sink}}$ guarantees that this participation does not generate a new anti-crossing, so the evolution remains smooth. In terms of evolution, the involvement of opposite-sign sectors allows the ground state to develop negative amplitudes in the computational basis. These arise from constructive and destructive interference between same-sign and opposite-sign components, a mechanism we refer to as *sign-generating quantum interference*. This interference-enabled path to the global minimum is inaccessible to stoquastic annealing, where amplitudes remain strictly nonnegative. The numerical confirmation of Stage 2 is given in Section 9.6 of Supplement.

Taken together, the two stages yield a smooth overall evolution: Stage 1 steers the system into the *R*-localized region without tunneling, and Stage 2 completes the transition to GM via an opposite-sign, interference-enabled path.

References and Notes

1. P. W. Shor, Polynomial-Time Algorithms for Prime Factorization and Discrete Logarithms on a Quantum Computer. *SIAM Journal on Computing* **26** (5), 1484–1509 (1997).
2. R. Babbush, *et al.*, The Grand Challenge of Quantum Applications. *arXiv preprint arXiv:2511.09124v3* (2025).
3. M. Dupont, *et al.*, Quantum-enhanced greedy combinatorial optimization solver. *Science Advances* **9** (45), eadi0487 (2023).
4. S. P. Jordan, *et al.*, Optimization by Decoded Quantum Interferometry. *Nature* **646**, 831–836 (2025).
5. V. Choi, Essentiality of the Non-stoquastic Hamiltonians and Driver Graph Design in Quantum Optimization Annealing. *arXiv preprint arXiv:2105.02110v2* (2021).
6. M. R. Garey, D. S. Johnson, *Computers and Intractability: A Guide to the Theory of NP-Completeness* (W. H. Freeman, San Francisco) (1979).
7. V. Choi, Minor-embedding in adiabatic quantum computation: I. The parameter setting problem. *Quantum Information Processing* **7** (5), 193–209 (2008).
8. V. Choi, Minor-embedding in adiabatic quantum computation: II. Minor-universal graph design. *Quantum Information Processing* **10** (3), 343–353 (2011).
9. M. W. Johnson, *et al.*, Quantum annealing with manufactured spins. *Nature* **473** (7346), 194–198 (2011).
10. S. Ebadi, *et al.*, Quantum optimization of maximum independent set using Rydberg atom arrays. *Science* **376** (6598), 1209–1215 (2022).
11. E. Farhi, J. Goldstone, S. Gutmann, M. Sipser, Quantum Computation by Adiabatic Evolution. *arXiv preprint quant-ph/0001106* (2000).
12. E. Farhi, *et al.*, A Quantum Adiabatic Evolution Algorithm Applied to Random Instances of an NP-Complete Problem. *Science* **292** (5516), 472–475 (2001).
13. H. Nishimori, *Statistical Physics of Spin Glasses and Information Processing: An Introduction* (Oxford University Press, Oxford, UK) (2001).
14. D. Aharonov, *et al.*, Adiabatic quantum computation is equivalent to standard quantum computation. *SIAM Journal on Computing* **37** (1), 166–194 (2007).
15. R. Barends, *et al.*, Digitized adiabatic quantum computing with a superconducting circuit. *Nature* **534** (7606), 222–226 (2016).
16. T. Albash, D. A. Lidar, Adiabatic quantum computation. *Rev. Mod. Phys.* **90**, 015002 (2018).
17. V. Choi, Beyond Stoquasticity: Structural Steering and Interference in Quantum Optimization. *arXiv preprint arXiv:2509.16263* (2025).
18. S. Lamm, P. Sanders, C. Schulz, D. Strash, R. F. Werneck, Finding Near-Optimal Independent Sets at Scale. *Journal of Experimental Algorithmics* **23**, 1–20 (2018).
19. S. Lamm, P. Sanders, C. Schulz, D. Strash, R. F. Werneck, KaMIS: An Exact Solver for the Maximum Independent Set Problem, in *Proceedings of the 18th Workshop on Algorithm Engineering and Experiments (ALENEX)* (2016).
20. K. Hukushima, K. Nemoto, Exchange Monte Carlo Method and Application to Spin Glass Simulations. *Journal of the Physical Society of Japan* **65** (6), 1604–1608 (1996).
21. J. Kempe, A. Kitaev, O. Regev, The Complexity of the Local Hamiltonian Problem. *SIAM Journal on Computing* **35** (5), 1070–1097 (2006).

22. I. Hen, Determining quantum Monte Carlo simulability with geometric phases. *Phys. Rev. Research* **3** (2), 023080 (2021).
23. H.-Y. Huang, S. Choi, J. R. McClean, J. Preskill, The Vast World of Quantum Advantage. *arXiv:2508.05720* (2025).
24. E. Farhi, J. Goldstone, S. Gutmann, A Quantum Approximate Optimization Algorithm. *arXiv:1411.4028* (2014).
25. V. Choi, Limitation of Stoquastic Quantum Annealing: A Structural Perspective. *arXiv preprint arXiv:2509.16265* (2025).

Acknowledgments

The author thanks Jamie Kerman for introducing her to the angular-momentum basis and for early discussions. The author also thanks Siyuan Han for helpful comments.

The author acknowledges support from the Defense Advanced Research Projects Agency under Air Force Contract No. FA8702-15-D-0001. Any opinions, findings and conclusions or recommendations expressed in this material are those of the author and do not necessarily reflect the views of the Defense Advanced Research Projects Agency.

Supplementary materials

Supplement consists of Sections 1–10, which correspond to Sections 1–10 of (17), and Section 11, which corresponds to Section 5 of (25).